

“El Niño Like” Hydroclimate Responses to Last Millennium Volcanic Eruptions

SAMANTHA STEVENSON, BETTE OTTO-BLIESNER, JOHN FASULLO, AND ESTHER BRADY

Climate and Global Dynamics Division, National Center for Atmospheric Research, Boulder, Colorado

(Manuscript received 31 March 2015, in final form 11 January 2016)

ABSTRACT

The hydroclimate response to volcanic eruptions depends both on volcanically induced changes to the hydrologic cycle and on teleconnections with the El Niño–Southern Oscillation (ENSO), complicating the interpretation of offsets between proxy reconstructions and model output. Here, these effects are separated, using the Community Earth System Model Last Millennium Ensemble (CESM-LME), by examination of ensemble realizations with distinct posteruption ENSO responses. Hydroclimate anomalies in monsoon Asia and the western United States resemble the El Niño teleconnection pattern after “Tropical” and “Northern” eruptions, even when ENSO-neutral conditions are present. This pattern results from Northern Hemisphere (NH) surface cooling, which shifts the intertropical convergence zone equatorward, intensifies the NH subtropical jet, and suppresses the Southeast Asian monsoon. El Niño events following an eruption can then intensify the ENSO-neutral hydroclimate signature, and El Niño probability is enhanced two boreal winters following all eruption types. Additionally, the eruption-year ENSO response to eruptions is hemispherically dependent: the winter following a Northern eruption tends toward El Niño, while Southern volcanoes enhance the probability of La Niña events and Tropical eruptions have a very slight cooling effect. Overall, eruption-year hydroclimate anomalies in CESM disagree with the proxy record in both Southeast Asia and North America, suggesting that model monsoon representation cannot be solely responsible. Possible explanations include issues with the model ENSO response, the spatial or temporal structure of volcanic aerosol distribution, or data uncertainties.

1. Introduction

Over the past millennium, volcanic eruptions create the largest nonanthropogenic perturbations to the climate system (see review by [Robock 2000](#)). Injection of aerosols into the lower stratosphere decreases surface downward solar radiation, suppressing the global hydrologic cycle and cooling the majority of Earth’s surface. Large eruptions make ideal test cases for evaluating the climate response to external forcing in global models used for future climate projections, but very few events have occurred since the start of the modern observational record. Historical eruptions are known to be much larger than more recent events, such as the Tambora eruption, which caused the famous 1815 “year without a summer” ([Stommel and Stommel 1983](#); [Stothers 1984](#)); for more robust statistics, information from paleoclimate archives must be included. The magnitude and location of past eruptions can be

estimated from geological evidence as well as archives such as sulfate aerosol deposits in ice cores, and several reconstructions of eruption strength have been created from such archives ([Gao et al. 2008](#); [Crowley et al. 2008](#); [Sigl et al. 2014](#)). The effects of eruptions can then be inferred using other sources of paleoclimate data: the most common come from terrestrial archives such as tree-ring widths, and much work has been performed on quantifying these influences in various locations [i.e., monsoon Asia and the North American west; [Anchukaitis et al. \(2010\)](#); [Li et al. \(2013\)](#)].

Model comparison with proxy data requires consideration of modes of internal climate variability, which are in turn impacted by eruptions. Climate modeling and proxy studies indicate that both the Atlantic multidecadal oscillation (AMO; [Knudsen et al. 2014](#); [Zanchettin et al. 2012](#); [Mignot et al. 2011](#)) and the interdecadal Pacific oscillation (IPO; [Maher et al. 2014](#)) respond to large eruptions, but the El Niño–Southern Oscillation (ENSO) has a stronger impact on temperature and precipitation in the tropics/midlatitudes. Some proxy evidence indicates that initiation of El Niño events is favored by volcanic eruptions in the year after

Corresponding author address: Samantha Stevenson, Climate and Global Dynamics Division, National Center for Atmospheric Research, 1850 Table Mesa Dr., Boulder, CO 80303.
E-mail: samantha@ucar.edu

the eruption (Adams et al. 2003; Li et al. 2013), which has been documented in climate models (Timmreck 2012) and is generally attributed to the oceanic “dynamical thermostat” mechanism (Clement et al. 1996); however, this result is subject to substantial internal variability (Emile-Geay et al. 2008). Some proxy evidence also exists for an immediate “La Niña like” tropical Pacific cooling period prior to the El Niño initiation, during the year in which the eruption occurs (Li et al. 2013); this effect is not simulated by most climate models (McGregor and Timmermann 2011) and has not been observed after twentieth-century eruptions. Although not all reconstructions agree on the eruption-year tropical Pacific cooling (Wahl et al. 2014), the inability of models to simulate this La Niña-like response has been attributed to issues with model representations of the Southeast Asian monsoon and of ENSO itself (Anchukaitis et al. 2010). The degree to which this discrepancy is caused by model error or data uncertainty thus remains an open question.

The recently completed Community Earth System Model Last Millennium Ensemble (CESM-LME; Otto-Bliesner et al. 2015) is an ideal toolkit for disentangling the direct hydroclimate response to eruptions from ENSO. The LME contains multiple realizations of the 850–2005 CE period run with identical forcing, meaning that the statistics of the volcanic–ENSO link may be investigated simply by selecting cases with differing ENSO conditions, without the need to consider differences in model physics or volcanic forcing. The model configuration and eruptions are described in section 2, the overall climate response to eruptions in the CESM is documented in section 3, the interaction between ENSO and the direct impact of an eruption is investigated in section 4, and implications for comparison with paleoclimate archives are discussed in section 5.

2. Model configuration and eruption selection

All results presented in this study utilize the LME (Otto-Bliesner et al. 2015); the model configuration used is the CESM1.1, the same model version used for the CESM Large Ensemble (Kay et al. 2015), but run at lower land and atmosphere resolution because of the more intensive computing time demands of the ensemble. Model resolution is roughly 2° in the atmosphere and land models, and varies from 1° to 0.3° in the ocean.

The LME consists of several different ensembles, forced either individually with solar insolation, orbital changes, land-use/land cover variations, volcanic eruptions, and greenhouse gases; or with all forcing factors simultaneously. Greenhouse gas concentrations (CO_2 , CH_4 , and N_2O) are derived from Antarctic ice cores (Schmidt et al. 2011), orbitally induced changes in

insolation are computed following Berger (1978) as a function of season and latitude, changes in total solar irradiance (TSI) follow Vieira et al. (2010), and land-use/land cover changes use a combined dataset derived from Pongratz et al. (2009) and Hurtt et al. (2011). The relevant forcings are applied identically across ensemble members, and ensemble spread is generated by perturbation of the atmospheric initial conditions; full details are available in Otto-Bliesner et al. (2015).

Volcanic eruptions in the LME use forcings derived from version 1 of the ice core–based reconstruction by (Gao et al. 2008), the same forcing dataset used in the CESM Last Millennium simulation for CMIP5 (Landrum et al. 2013). Aerosol concentration varies as a function of latitude, altitude, and time. The latitudinal distribution is prescribed using nine latitude bands (Gao et al. 2008), as well as the exchange between the latitude bands computed using a simplified transport model (Grieser and Schonwiese 1999) including seasonal variations in stratospheric circulation. The three model layers just above the tropopause are used to prescribe volcanic aerosols, which are assumed to follow a single size distribution. The change in tropical clear-sky albedo resulting from all eruptions is shown in Fig. 1; hereafter, the year in which aerosol loading peaks is referred to as year 0. In the majority of cases, the profiles have very similar shapes as a result of the use of the Grieser and Schonwiese (1999) parameterization to derive the aerosol distribution; also, all eruptions with unknown seasonality are assumed to begin in April. The implications of eruption seasonality will be discussed further in section 5.

Here, we analyze output from the “full forcing” and “volcanic only” ensembles, consisting of nine and five simulations, respectively; one of the full-forcing members could not be fully analyzed owing to file loss, but all other members mentioned in Otto-Bliesner et al. (2015) are included. The full-forcing simulations contain all forcing factors described in the preceding paragraph, while the volcanic-only simulations exclude influences other than volcanic aerosols. Analysis has been restricted to the period 850–1850 to prevent inclusion of any CO_2 -induced hydroclimate trends that might skew the full-forcing results. Eruptions are divided into three general classes according to their hemispheric aerosol distribution, as computed by Gao et al. (2008). This was done by integrating the aerosol mass mixing ratio during the eruption year and two subsequent years over the Northern and Southern Hemispheres, then computing the ratio between the two. Eruptions with a ratio greater than 1.3 or less than 0.7 are classified as “Northern” and “Southern” eruptions, respectively; those with intermediate values are considered “Tropical.” To minimize biases from eruption size variations, only eruptions with a peak aerosol mass

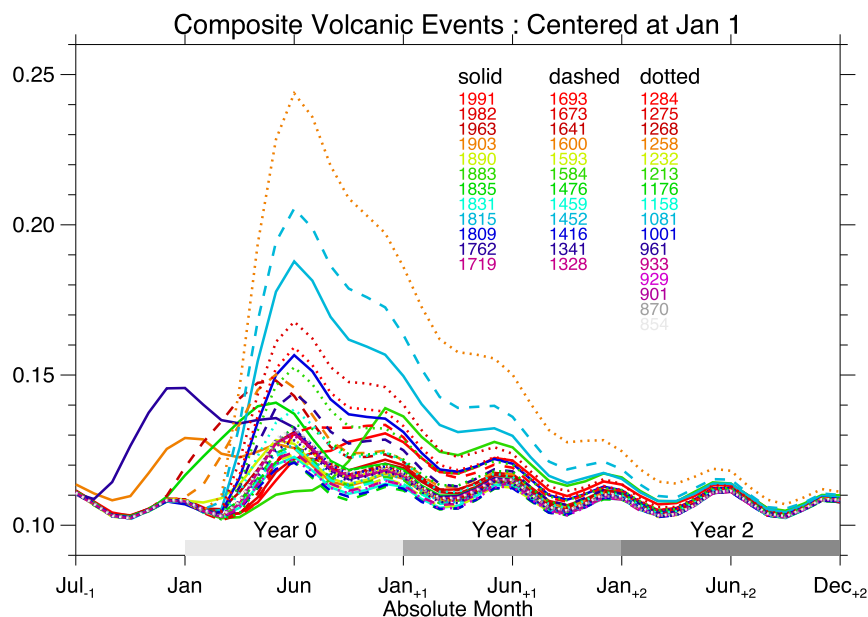


FIG. 1. Composite clear-sky albedo for all LME eruptions, averaged over ocean regions from 30°S to 30°N. Eruptions occurring after 1700 are represented by solid lines, eruptions occurring between 1300 and 1699 by dashed lines, and eruptions occurring before 1300 by dotted lines. The eruption year indicated here is the year in which the albedo reaches its peak; this is the year referred to as year 0 in subsequent analyses.

mixing ratio greater than 10^{-8} were included in the final sample; the resulting list is given in Table 1.

3. Climate response to eruptions

The global response to eruptions in the LME is consistent with results from previous studies (Schneider et al. 2009), as documented in Fig. 2. Figures 2a and 2b show the composite hemispheric-mean anomaly in surface net solar radiation as a function of time after eruptions of various classes; in all cases there is a decrease that lasts for an average of 1–3 yr. The Tropical eruptions have comparable excursions in Northern and Southern Hemisphere fluxes, and are generally stronger than the hemisphere-dominant events. Northern eruptions show the strongest latitudinal temperature gradient shift (Figs. 2e,f); the other two categories create cooling at both the tropics and high latitudes. Across eruption classes, the temperature anomaly ranges from -1° to -6°C in a zonal-mean sense (Figs. 2c–h), with the largest anomalies in the Northern Hemisphere high latitudes. Temperature effects generally become negligible after 2–3 yr in the tropics, with persistence time scales of up to 10 yr poleward of 50°N; this is likely due to feedbacks with Arctic sea ice (Schneider et al. 2009). Unless otherwise specified, the 12-month climatological-mean annual cycle over 850–1849 has been removed from the monthly data prior to compositing.

Composite patterns of the December–February (DJF) temperature response to eruptions are shown in Fig. 3; these and subsequent composites show the mean across all full-forcing and volcanic-only simulations. Consistent with the zonal-mean plots in Fig. 2, cooling occurs nearly everywhere, with the exception of a small portion of northern Europe (not shown). Cooling is strongest everywhere over land, with anomalies reaching up to -5°C in some portions of North America and the mountain regions of Asia, and the effects are strongest during year 0. Composite precipitation patterns are shown in Fig. 4; during DJF

TABLE 1. List of eruption years belonging to the Tropical, Northern, and Southern eruption classes. Eruptions between 850 and 1850 having peak global-mean aerosol mass mixing ratios above 1×10^{-8} are included here. *The Laki eruption was assigned an incorrect date in the Gao et al. (2008) version 1 dataset; the true date is 1783. **Eruptions are classed by the ratio of Northern to Southern Hemisphere stratospheric aerosol loading over the course of the eruption, as quantified by Gao et al. (2008); ratios above 1.3 are considered Northern, those below 0.7 are considered to be Southern, and those between 0.71 and 1.29 are Tropical according to this classification.

Class**	Years
Tropical	1258 (Samalas), 1284, 1809, 1815 (Tambora)
Northern	1176, 1213, 1600, 1641, 1762 (Laki*), 1835
Southern	1275, 1341, 1452 (Kuwae)

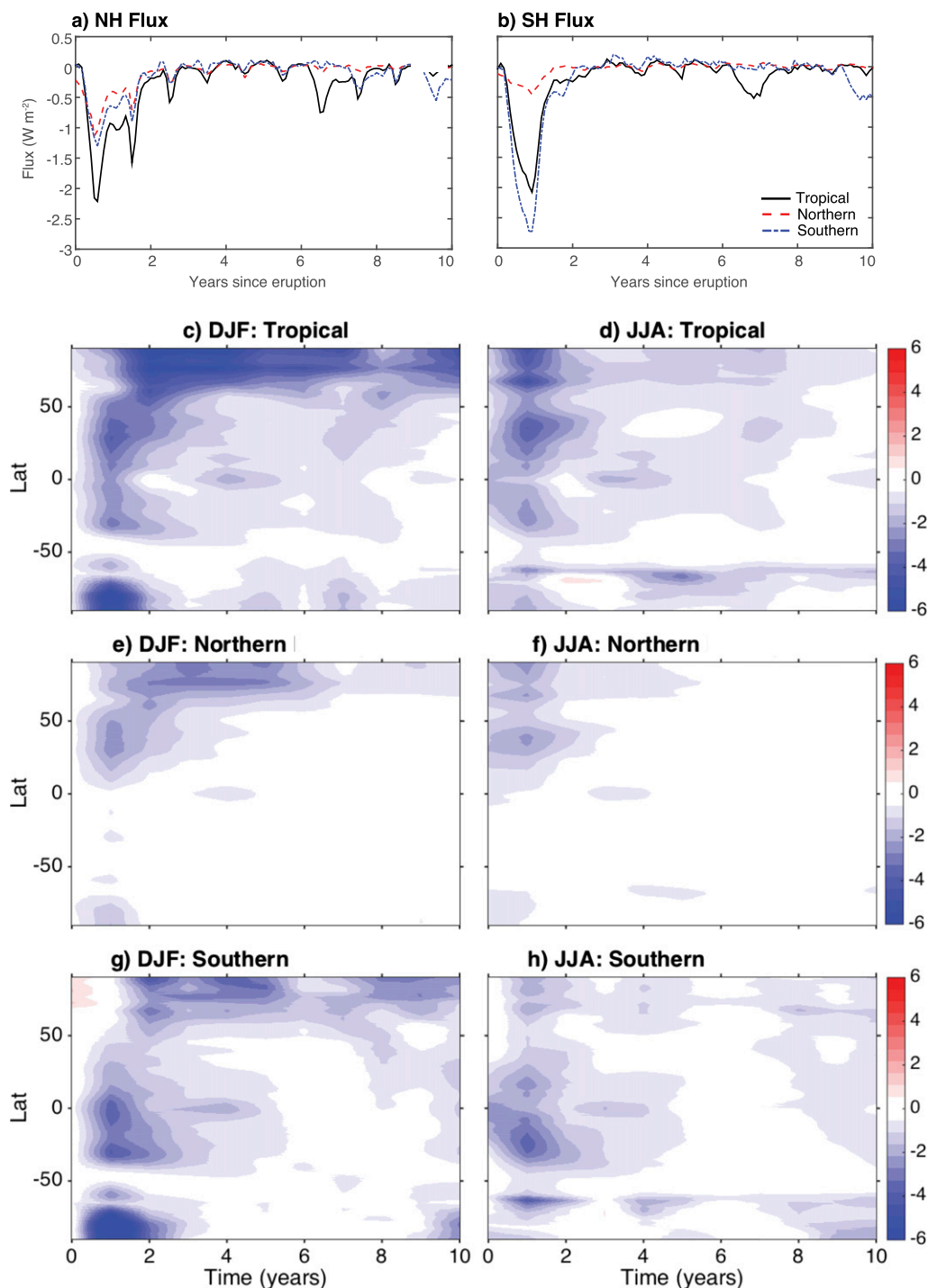


FIG. 2. Response of solar flux and surface temperature to eruptions in the LME full-forcing ensemble. (a),(b) Net solar flux anomaly at surface in the Northern and Southern Hemispheres, for all three eruption classes. (c),(d) Zonally averaged temperature anomaly ($^{\circ}\text{C}$) for Tropical eruptions, during (c) DJF and (d) JJA. (e),(f) As in (c),(d), but for Northern eruptions. (g),(h) As in (c),(d), but for Southern eruptions. All anomalies are calculated relative to the 850–1850 mean.

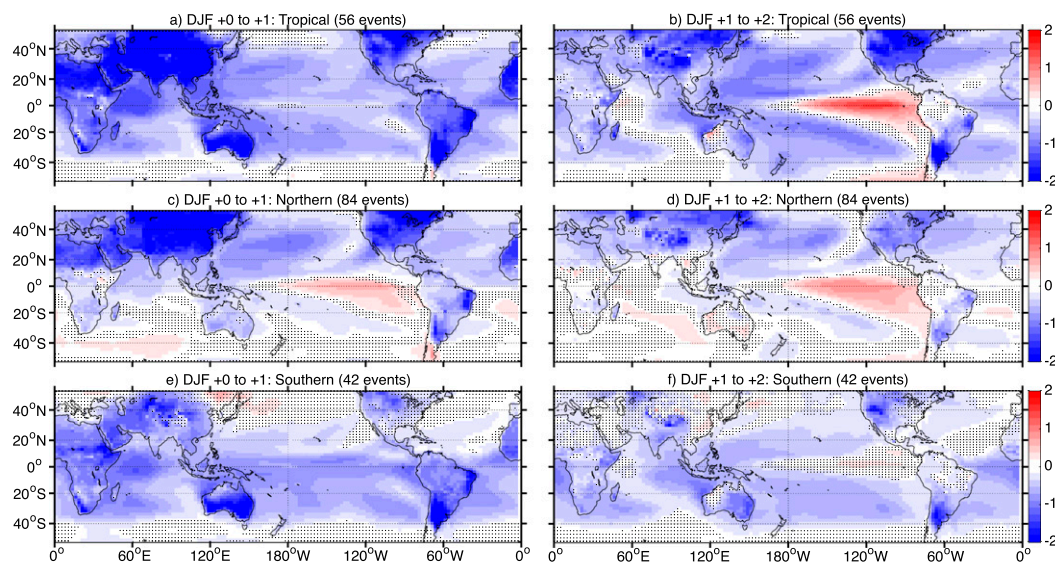


FIG. 3. Composite surface air temperature response ($^{\circ}\text{C}$) to eruptions of varying sizes: (a),(b) Tropical, (c),(d) Northern, and (e),(f) Southern eruptions. The left-hand column [(a),(c),(e)] indicates responses during DJF of years +0 to +1. The right-hand column [(b),(d),(f)] indicates responses during DJF of years +1 to +2. Significance levels are determined according to the Wilcoxon rank-sum test, and values that are insignificant at 90% are stippled.

of years 0 to +1 (Figs. 4a,c,e), reduced rainfall occurs over land, particularly in the tropics (the western United States and parts of South America are exceptions). Strong changes are also observed over the ocean, with a dipolar signature centered along the equator consistent with an equatorward (poleward) migration of the

intertropical convergence zone (ITCZ) for Northern (Southern) eruptions.

The climate response in years +1 to +2 differs from that in years +0 to +1. During DJF +0 to +1, the Tropical eruptions show little change in temperature in the eastern equatorial Pacific (Fig. 3a). A net warming is

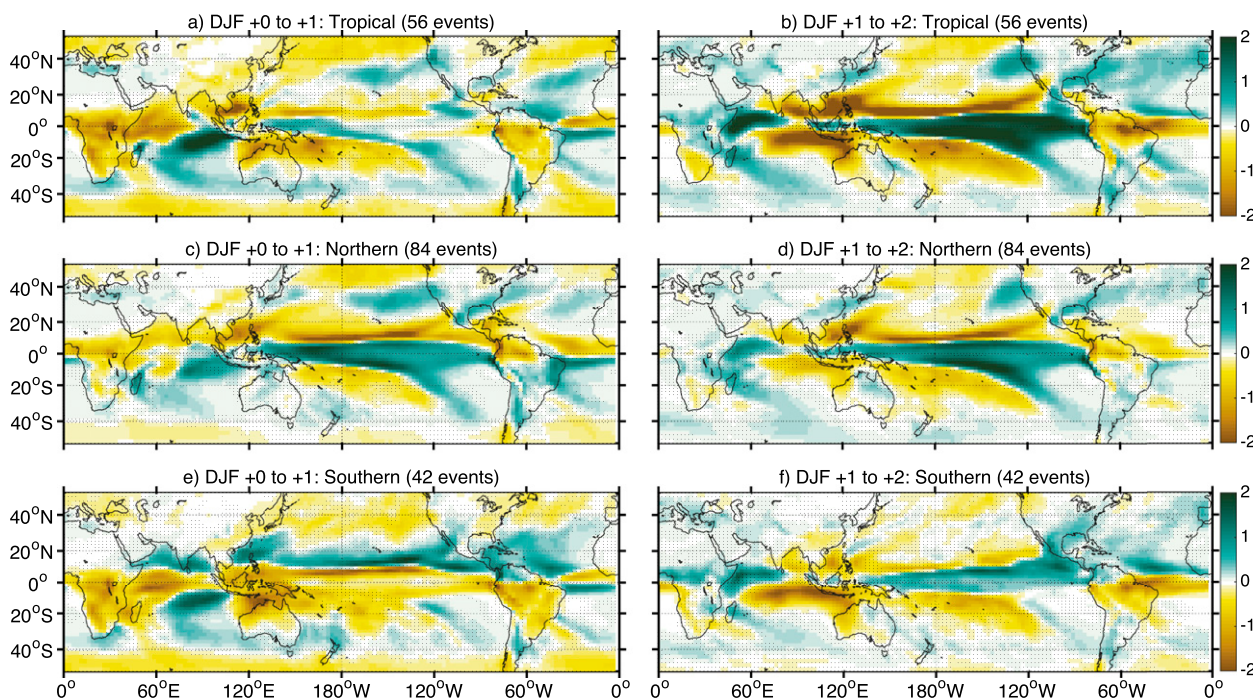


FIG. 4. As in Fig. 3, but for total precipitation (mm day^{-1}).

TABLE 2. Probability of occurrence for El Niño and La Niña events during DJF, for eruptions of all classes. Boldface entries indicate occurrence frequencies lying outside the 90% confidence interval derived from the LME 850 control simulation, the upper and lower limits of which (95th and 5th percentiles, respectively) are listed in the control rows.

	Neutral	El Niño	La Niña
Tropical, DJF 0 to 1	67.8	12.5	19.6
Tropical, DJF 1 to 2	53.6	41.1	5.36
Northern, DJF 0 to 1	69.1	22.6	8.33
Northern, DJF 1 to 2	64.3	28.6	7.14
Southern, DJF 0 to 1	50.0	9.52	40.5
Southern, DJF 1 to 2	66.7	21.4	11.9
Control, 5th percentile	68.5	13.8	11.8
Control, 95th percentile	73.1	17.6	15.2

seen in response to the Northern eruptions (Fig. 3c), along with a cooling in response to Southern eruptions (Fig. 3e). However, during DJF +1 to +2, a pronounced El Niño-like pattern appears in both temperature and precipitation for Tropical and Northern eruptions (Figs. 3 and 4b,d); the eastern equatorial Pacific warms substantially, and the ITCZ signature is much stronger than during DJF +0 to +1 in both cases.

A summary of the likelihood of El Niño–La Niña occurrence after eruptions of all strengths is shown in Table 2. Hereafter, El Niño and La Niña events are defined as Niño-3.4 SST anomalies exceeding ± 1 standard deviation from the ensemble-member mean; the results are similar when other thresholds are adopted (not shown). During DJF of years 0 to +1, cool conditions in the equatorial Pacific are favored for Southern eruptions and to a lesser extent for Tropical eruptions; Northern eruptions tend to enhance El Niño occurrence. During DJF of years +1 to +2, however, both Tropical and Northern eruptions have dramatically increased the probabilities of El Niño occurrence and decreased the probability of La Niña occurrence. Changes are statistically significant for all eruption classes across the ensemble.¹

The mechanism for the hemispheric dependence of the ENSO response to volcanism is not yet clear. El Niño initiation may be favored by equatorward migration of the ITCZ and associated trade wind weakening, which is shown (section 4) to be strongest for Northern eruptions. The reverse may be true for Southern eruptions, which could explain the enhanced La Niña probability after Southern events. We note that the temperature pattern in

Fig. 3e appears not to be strictly analogous to La Niña initiation, but for these purposes a colder than average SST is referred to as being La Niña like. The dynamics of this response are left for future investigation. Another caveat is that the ENSO amplitude in CESM is too strong as compared with the observations, although CESM exhibits a much more realistic and broad spectral peak than previous model versions (Fig. 5); this overly strong amplitude could become important when interactions between ENSO and direct volcanic impacts are considered (section 4).

4. El Niño-induced amplification

The question of volcanic influences on ENSO has important implications for the interpretation of the terrestrial proxy record. As such, the Palmer drought severity index (PDSI; Palmer 1965) has been computed from CESM output using a modified version of the toolbox presented in Jacobi et al. (2013). The PDSI is the canonical quantity to which records of tree-ring width are typically calibrated, and represents an approximation of the water balance in the upper soil layer. The PDSI calculation here relies on potential evapotranspiration computed using the Penman–Monteith method; comparisons with CESM soil moisture (not shown) reveal that PDSI is correlated at $R = 0.8$ – 0.9 with soil moisture in the upper 50 cm to 2 m, on interannual time scales. This result is consistent with computations from other climate models (Cook et al. 2015) and indicates that PDSI robustly reflects changes in modeled hydrological conditions. Here, June–August (JJA) PDSI values are reported, for consistency with the North American and monsoon Asia drought atlases (NADA and MADA, respectively; Cook et al. 2004, 2010); because of the memory of 9–12 months present in PDSI, this quantity can be considered to represent hydrological conditions during the previous year.

PDSI composites following eruptions are shown in Fig. 6, for JJA of years +1 and +2. The ENSO teleconnection pattern is also shown for comparison (Figs. 6a,b) using composite JJA PDSI values 6 months following El Niño–La Niña events in the LME 850 control run. After Tropical and Northern eruptions, drying is observed over monsoon Asia and wetting over the southwest United States, which persist in both years +1 and +2 (Figs. 6c–f). There are distinct similarities between these patterns and the El Niño teleconnection in Fig. 6a, as shown by the strong positive pattern correlations (numerical values in Figs. 6c–f). Southern eruptions do not produce El Niño-like PDSI patterns, or indeed any significant PDSI excursions, in either monsoon Asia or the southwest United States. Outside of the boxed regions in Fig. 6, there is very little correspondence between eruption and El Niño

¹ Statistical significance is computed using the nonparametric Wilcoxon rank-sum test (“ranksum” in Matlab), in which the set of posteruption values is compared with the full time series from all ensemble members, on a gridpoint by gridpoint basis.

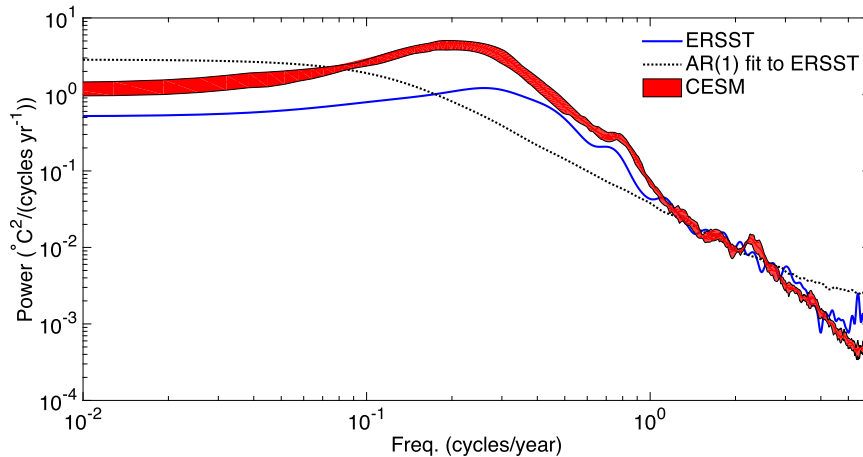


FIG. 5. Niño-3.4 SST anomaly power spectrum for the LME full-forcing ensemble. The SSTA spectrum for the ERSSTv3b data product (Smith et al. 2008) is indicated by the blue solid line, and the red envelope shows the 25th–75th percentile range for the LME simulations. An AR(1) spectrum fitted to ERSST is shown in black, as a null hypothesis.

hydroclimate signatures, with the possible exception of Europe, portions of the Middle East, and midlatitude South America (20°–40°S). The dynamics of eruption influences are clearly distinct from ENSO teleconnection signatures.

Both Northern and Tropical eruptions favor El Niño initiation, so the degree to which El Niño events generate the El Niño-like PDSI signatures in the boxed regions of Fig. 6 (hereafter the NA and MA boxes in North America and monsoon Asia, respectively) is investigated next. Events within an eruption class are categorized according to the ENSO state: either El Niño or ENSO neutral during DJF +0 to +1, and the resulting JJA +1 PDSI shown in Fig. 7. (Note that within the ENSO-neutral category, the mean Niño-3.4 value is roughly -0.3°C , so the ENSO-neutral composite is not likely to be biased toward an El Niño teleconnection). Pattern correlations are computed between the ENSO-neutral PDSI and the El Niño teleconnection map for all eruption types: correlations for the Tropical eruptions are 0.75–0.76 (Fig. 7a) and 0.70–0.82 for the Northern eruptions (Fig. 7c) in the MA and NA boxes, respectively. This is an indication that the correspondence between the eruption and El Niño teleconnection PDSI signatures arise from non-ENSO processes. Results are similar for JJA +2, although the ENSO-neutral influence weakens considerably (not pictured).

The presence of El Niño conditions appears to amplify the hydroclimate signature of a volcanic eruption, in both monsoon Asia and the North American southwest. This is apparent visually by comparing Figs. 7a,b and 7c,d; the effect is then quantified using the mean PDSI in the boxed regions of Fig. 7. For Tropical eruptions,

the mean PDSI values in monsoon Asia are increased by a factor of 1.74 in the presence of El Niño conditions relative to the ENSO-neutral composite; in North America the amplification factor is 2.88. For Northern eruptions, El Niño conditions amplify PDSI in monsoon Asia by a factor of 1.44 and in North America by a factor of 2.24.

Based on Figs. 6 and 7, it is clear that ENSO teleconnections and ENSO-neutral eruption influences must be understood individually; the mechanisms for similarities over MA and NA are investigated below.

a. Subtropical tropospheric jet

Both volcanic eruptions and ENSO variability affect the midlatitude tropospheric jets. In the case of ENSO, Seager et al. (2003) showed that tropical heating during El Niño events creates an equatorward shift and intensification of the jets, while the reverse is true for a La Niña. Eruptions are also known to affect the zonal-mean circulation through modification of the meridional temperature gradient (Robock 2000; Schneider et al. 2009). We note that in the stratosphere, the volcanic and ENSO responses differ dramatically (not pictured), as aerosol-induced stratospheric heating makes up a key portion of the volcanic response, but a similar uniform stratospheric heating is generally not induced by ENSO dynamics alone.

Figure 8 shows the composite zonal-mean zonal wind anomalies from 1000 to 500 mb, for volcanic eruptions of varying sizes accompanied by various ENSO phases during DJF +0 to +1. ENSO-neutral eruptions lead to an equatorward shift of the jet, as evidenced by the westerly wind anomalies on the equatorward flank of the

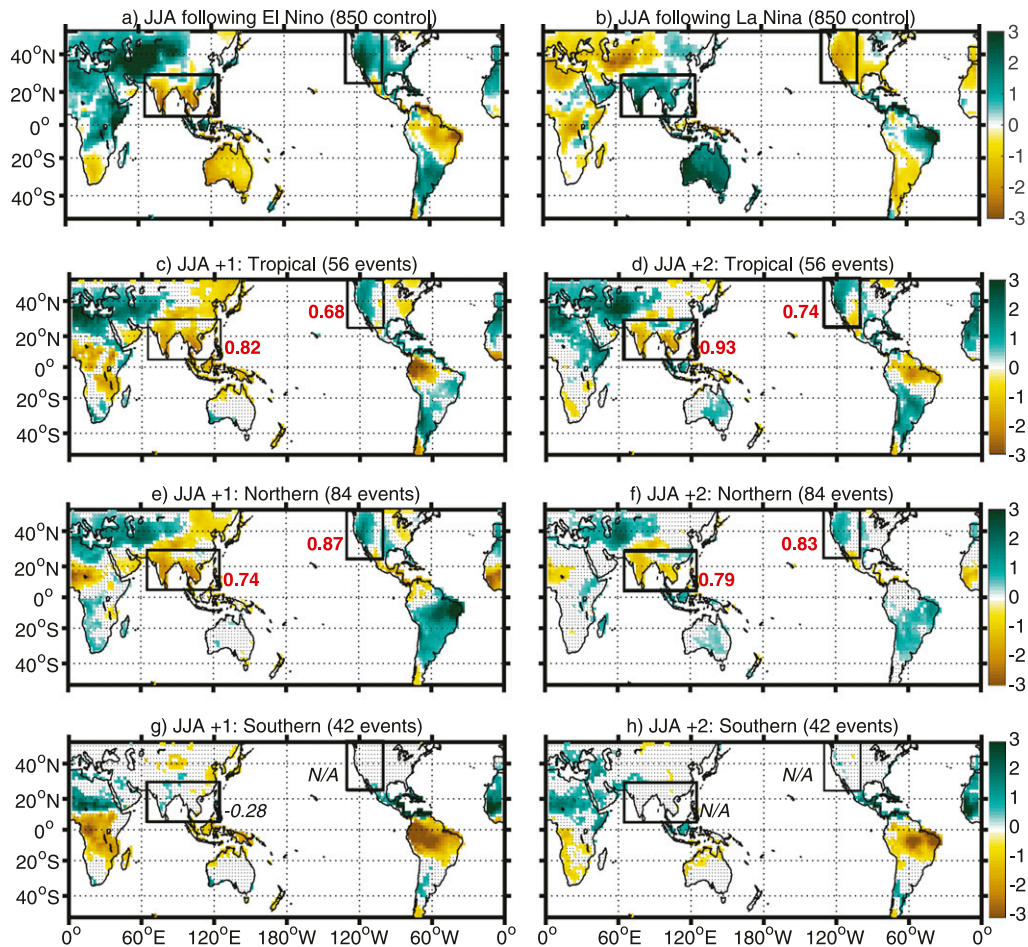


FIG. 6. JJA PDSI composites for (a) El Niño events in the LME 850 control run. (b) La Niña events in the LME 850 control run. (c)–(h) Eruptions of varying types over 850–1850 in the LME full-forcing ensemble. JJA of Year +1 is shown in the left-hand column; JJA of year +2 is shown in the right-hand column. No filtering based on ENSO phase has been performed in (c)–(h). Only regions where the PDSI anomaly following the eruption [or El Niño/La Niña event, in (a),(b)] differs significantly from the full simulation, according to the Wilcoxon rank-sum test, are plotted. Boxes indicate the southwest United States and monsoon Asia regions discussed in the text, and the numbers alongside the boxes in (c)–(h) are the pattern correlations between the PDSI composite and the El Niño teleconnection in (a). Boldface red text indicates a pattern correlation significant at 95% relative to internal variability, as computed via a Wilcoxon rank-sum test. Italicized black text indicates an insignificant pattern correlation.

climatological-mean westerly jet (cf. positive anomalies near 20°N in Figs. 8c,f,i). This is interpreted as a consequence of the thermal wind relationship: volcanic cooling is stronger in the high latitudes, leading to an enhanced equator-to-pole temperature gradient and tending to accelerate the westerlies while enhancing baroclinic instability closer to the equator. Aerosol hemispheric loading appears to affect the magnitude of this effect: neutral Northern eruptions (Fig. 8f) show larger westerly anomalies near 20°–30°N than neutral Tropical or Southern eruptions (Figs. 8c–i). Likewise, neutral Southern eruptions (Fig. 8i) show larger westerly anomalies near 20°S than neutral Tropical/Northern eruptions (Figs. 8c,f).

The effect of a posteruption El Niño event is to amplify the NH westerly jet. Comparing Figs. 8a,d,g to 8c,f,i clearly shows that the westerly anomalies near 40°N and S are much stronger than those in the ENSO-neutral cases. The equatorial heating accompanying an El Niño event and the high-latitude cooling during an eruption alone both increase the meridional temperature gradient, while the opposite is true after eruptions followed by La Niña.

b. ITCZ shifts

The NH meridional temperature gradient responds similarly to ENSO-neutral eruptions and El Niño events

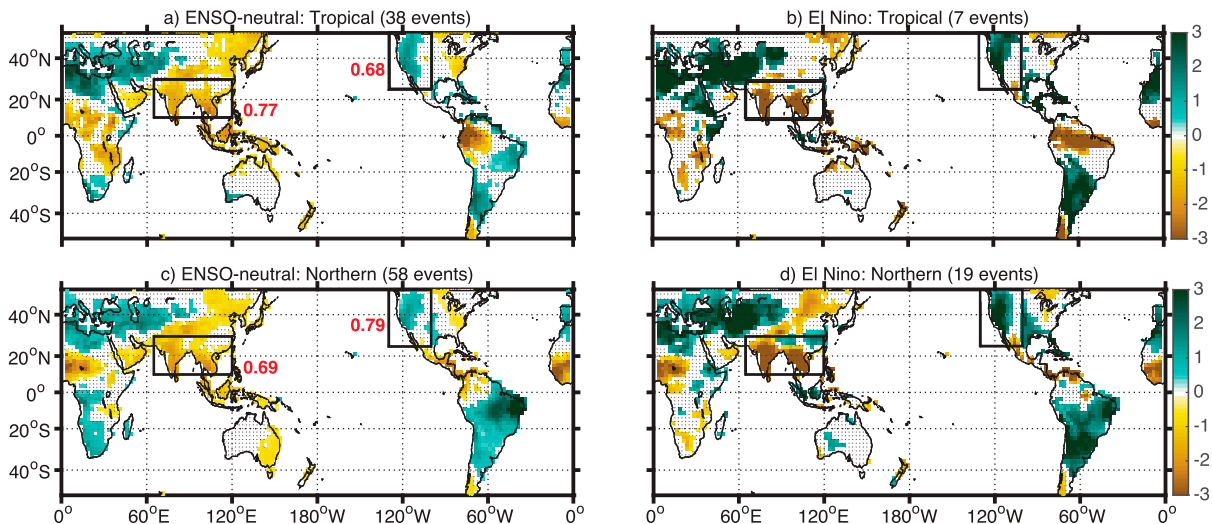


FIG. 7. PDSI composites for Tropical and Northern eruptions during JJA +1. (a) Tropical eruptions followed by ENSO-neutral conditions during DJF +0 to +1. (b) As in (a), but for eruptions followed by El Niño conditions. (c) Northern eruptions followed by ENSO-neutral conditions during DJF +0 to +1. (d) As in (c), but for eruptions followed by El Niño conditions. Boxes indicate the southwest United States and monsoon Asia regions discussed in the text, and the numbers alongside are the pattern correlations between the PDSI composite and the El Niño teleconnection pattern over the appropriate region. Boldface red text indicates a pattern correlation significant at 95% relative to internal variability, as computed via a Wilcoxon rank-sum test.

for Tropical/Northern eruptions. This is expected to create corresponding changes in ITCZ position, since the ITCZ tends to shift toward the equator during El Niño events and toward the warmer hemisphere in response to meridionally asymmetrical heating changes (Kang et al. 2008). Figure 9 shows the zonally averaged precipitation from 30°S to 30°N, with 1σ envelopes surrounding the (full + volcanic only) ensemble mean. Eruptions followed by ENSO-neutral conditions are shown in black, by El Niño conditions in red, and by La Niña conditions in blue. During DJF +0 to +1, the ENSO-neutral ITCZ shift is largest for Northern eruptions (Fig. 9d, black dashed), which exhibit a slight southward shift; for Tropical (Fig. 9a) and Southern eruptions (Fig. 9g), the ENSO-neutral ITCZ shifts are minimal. For all eruption classes, the phase of ENSO has a stronger impact on the ITCZ position than the ENSO-neutral aerosol forcing; eruptions followed by El Niño show a southward shift, and eruptions followed by La Niña northward (cf. red–blue envelopes in Figs. 9a,d,g). During JJA +1 the ENSO-neutral response is stronger than in DJF +0 to +1, and is dominated by a reduction in mean precipitation (Fig. 9b,e,h; gray envelope). Overall enhancement in ITCZ precipitation occurs during DJF +1 and 2 (Fig. 9c,f,i; gray envelope).

c. Asian monsoon suppression

The final similarity noted between ENSO-neutral eruptions and El Niño events is in the region dominated by the Asian monsoon. Figure 10 shows JJA +1

anomalies in precipitation and 850-hPa wind for all eruption classes, stratified by the ENSO phase during the previous boreal winter. The strongest circulation anomaly in the ENSO-neutral cases (Figs. 10c,f,i) is an anticyclonic pattern centered over India, associated with anomalous easterlies near 70°–90°E and tending to suppress the Somali jet and associated onshore flow into Southeast Asia. The fact that this circulation pattern is seen in all of the ENSO-neutral panels in Fig. 10 suggests that it relates to the direct response to volcanic aerosol forcing.

When ENSO acts in concert with a volcanic eruption, the results can differ dramatically depending on phase. By far the strongest reduction in precipitation is seen for cases where El Niño occurs in DJF +0 to +1; Figs. 10a,d,g all show drier conditions over the majority of Southeast Asia, and these dry anomalies persist strongly into JJA +2 for eruptions where El Niño conditions occur during DJF +1 to +2 (not shown). This reduction in precipitation is expected based on the reduced Walker circulation associated with El Niño conditions, which inhibits the ascending branch of the Indian and Southeast Asian monsoon circulations (Kumar et al. 2006). La Niña conditions seem to have impacts opposing the direct volcanic response; a strong westerly Somali jet is seen in Figs. 10e,h, as opposed to the easterly anomalies occurring in the El Niño case. Tropical eruptions followed by La Niña still exhibit easterly flow south of India (Fig. 10b), which might reflect the stronger aerosol loading associated with these eruptions. Notably, little change in monsoon precipitation is caused by ENSO-neutral Southern eruptions (Fig. 10i),

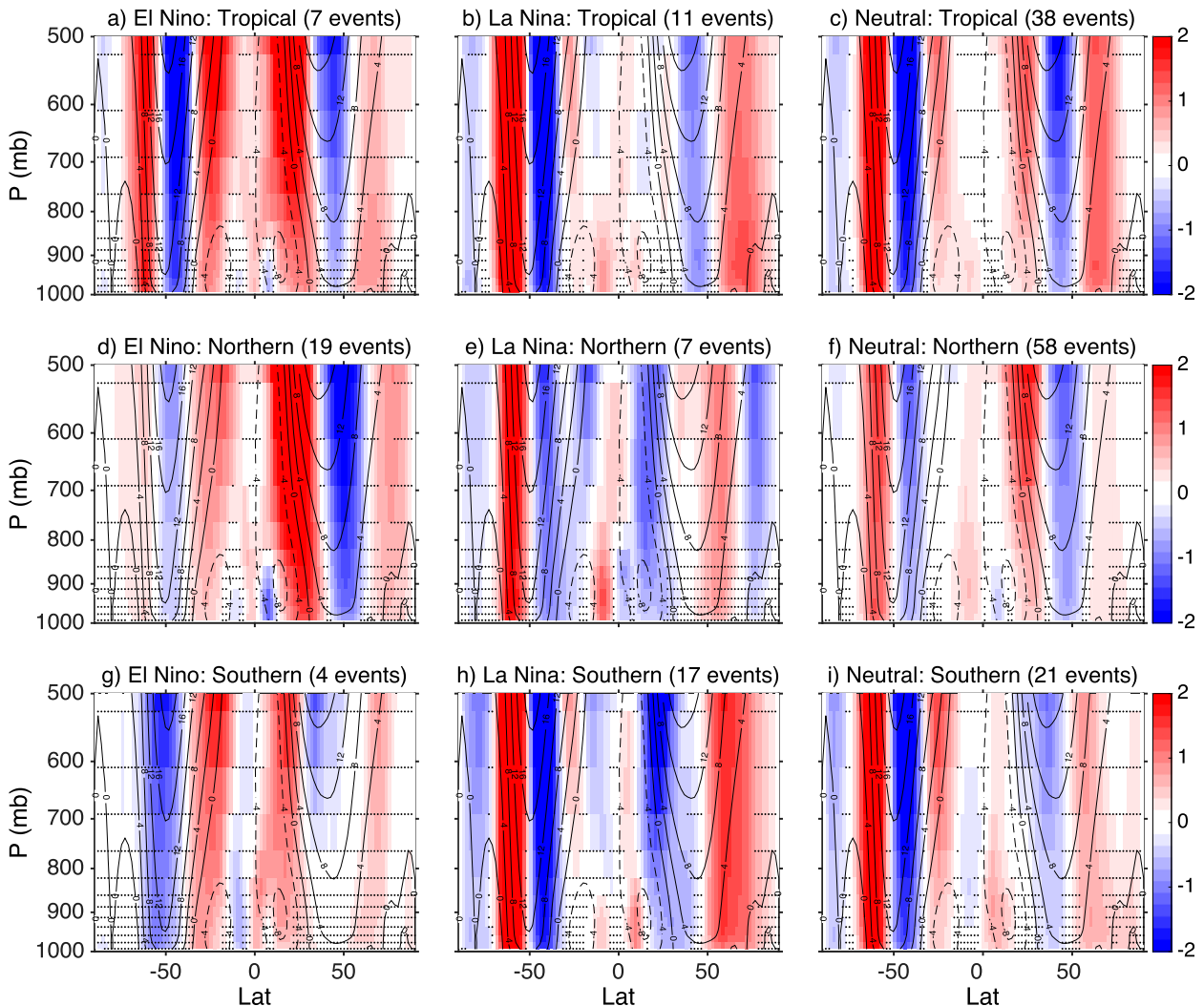


FIG. 8. Zonal-mean zonal wind averaged over the entire LME full-forcing ensemble (contours) and the anomaly composited over DJF of years +0 to +1 following eruptions of varying sizes (colors), sorted by ENSO phase. (a),(d),(g) El Niño conditions for Tropical, Northern, and Southern eruptions. (b),(e),(h) As in (a),(d),(g), but for eruptions followed by La Niña events. (c),(f),(i) As in (a),(d),(g), but for eruptions followed by ENSO-neutral conditions. Stippled areas indicate regions where the anomaly following the eruption does not differ significantly from the full simulation, according to the Wilcoxon rank-sum test. Units of mean and anomaly are m s^{-1} .

potentially because of the weaker land surface cooling over Asia during these events.

5. Comparison with tree-ring archives

The ultimate goal of this work is to determine whether CESM is capable of reproducing the responses to volcanic eruptions recorded in proxy archives and, if not, to attribute causes for model/proxy disagreements. As such, the PDSI composites from LME eruptions are compared with the North American and monsoon Asia drought atlases of Cook et al. (2004, 2010). The year +1 responses are quite similar between CESM (Fig. 6) and the proxy data (not shown); drying occurs in Southeast

Asia and wetting in the western United States in both the NADA/MADA and CESM, although CESM tends to slightly overestimate the PDSI anomaly values.

Previous work (Anchukaitis et al. 2010; Li et al. 2013) has shown that the eruption-year PDSI signature resembles a La Niña event, with wetting in monsoon Asia and drying in the western United States, while the year after the eruption generally shows the reverse. This result is reproduced in Fig. 11 for the NADA and MADA when the eruption years in Table 1 are used, but the CESM results contrast with the tree-ring composites; both Tropical and Northern eruptions show robust trends toward drying in Asia and wetting in the United States.

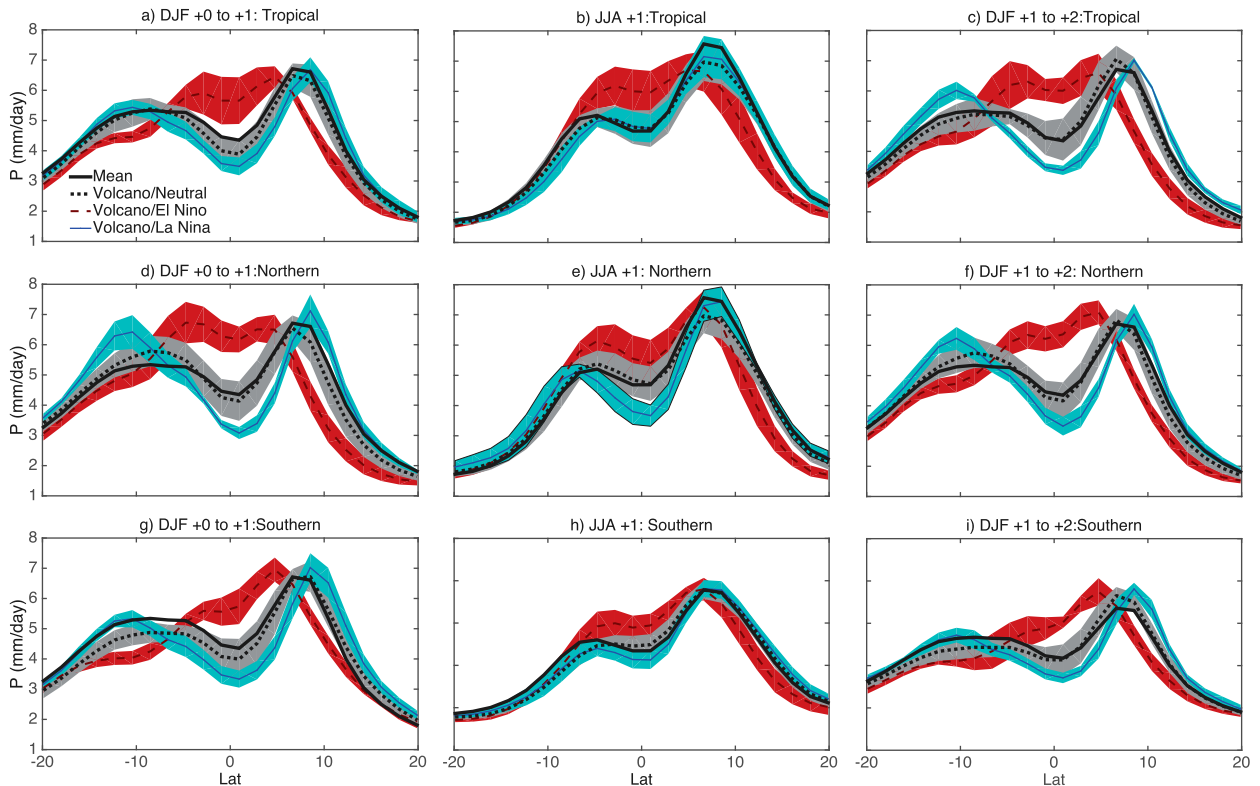


FIG. 9. Zonal-mean tropical precipitation (including both land and ocean) composited over DJF +0 to +1, JJA +1, and DJF +1 to +2 following eruptions of varying sizes, sorted by ENSO phase. (a)–(c) Tropical eruptions. (d)–(f) As in (a)–(c), but for Northern eruptions. (g)–(i) As in (a)–(c), but for Southern eruptions. In each panel, black solid lines indicate the ensemble mean (climatology), black dashed lines show eruptions followed by ENSO-neutral conditions, red dashed lines show eruptions followed by El Niño conditions, and blue dashed lines show eruptions followed by La Niña conditions. Envelopes surrounding each ensemble mean indicate the 1σ range for each set of events.

This work cannot definitively attribute causes for model/proxy offsets, as the experimental configuration here does not allow for the isolation of all influences, which could potentially cause disagreements with observations. Other possible complicating factors include the following:

- 1) An overly vigorous hydroclimate sensitivity to aerosol loading—[section 4](#) demonstrated that even in the absence of substantial tropical Pacific SST anomalies, the influence of volcanic aerosol forcing on hydroclimate bears a resemblance to the El Niño teleconnection pattern. If this effect is stronger in CESM than in reality, it would tend to mask an initial La Niña-like hydroclimate signature and lead to an overly large model/proxy disagreement during year 0.
- 2) An overestimate of the strength of eruptions—there are substantial uncertainties in ice core-derived reconstructions, in terms of size distribution, vertical loading profiles, and posteruption transport ([Gao et al. 2008](#)). If aerosol loading estimates are too large even for a few of the eruptions (as hypothesized by [Sigl et al. 2014](#)), [section 4](#) suggests that this would also create an erroneously El Niño-like hydroclimate pattern in the tropics/midlatitudes.
- 3) Issues with implementation of aerosol loading—the [Gao et al. \(2008\)](#) forcing dataset may not correctly account for interhemispheric aerosol differences, which have been demonstrated in [section 4](#) to play a strong role in shifting hydroclimate anomalies. Another potential issue is volcanic seasonality; in the [Gao et al. \(2008\)](#) reconstruction, all eruptions whose true seasonality was unknown were assumed to begin in April. This leads to a predominance of eruptions which peak during June–July, as shown in the clear-sky albedo during all eruptions in [Fig. 1](#). If modeled eruption aerosol injection peaks predominantly during boreal summer, this may be too late to create a significant influence on ENSO.
- 4) Issues with ENSO amplitude in the model—the ENSO amplitude in CESM is roughly a factor of 2 stronger than observed ([Fig. 5](#)), and the overall skewness is positive (not pictured). This creates a tendency for overly strong

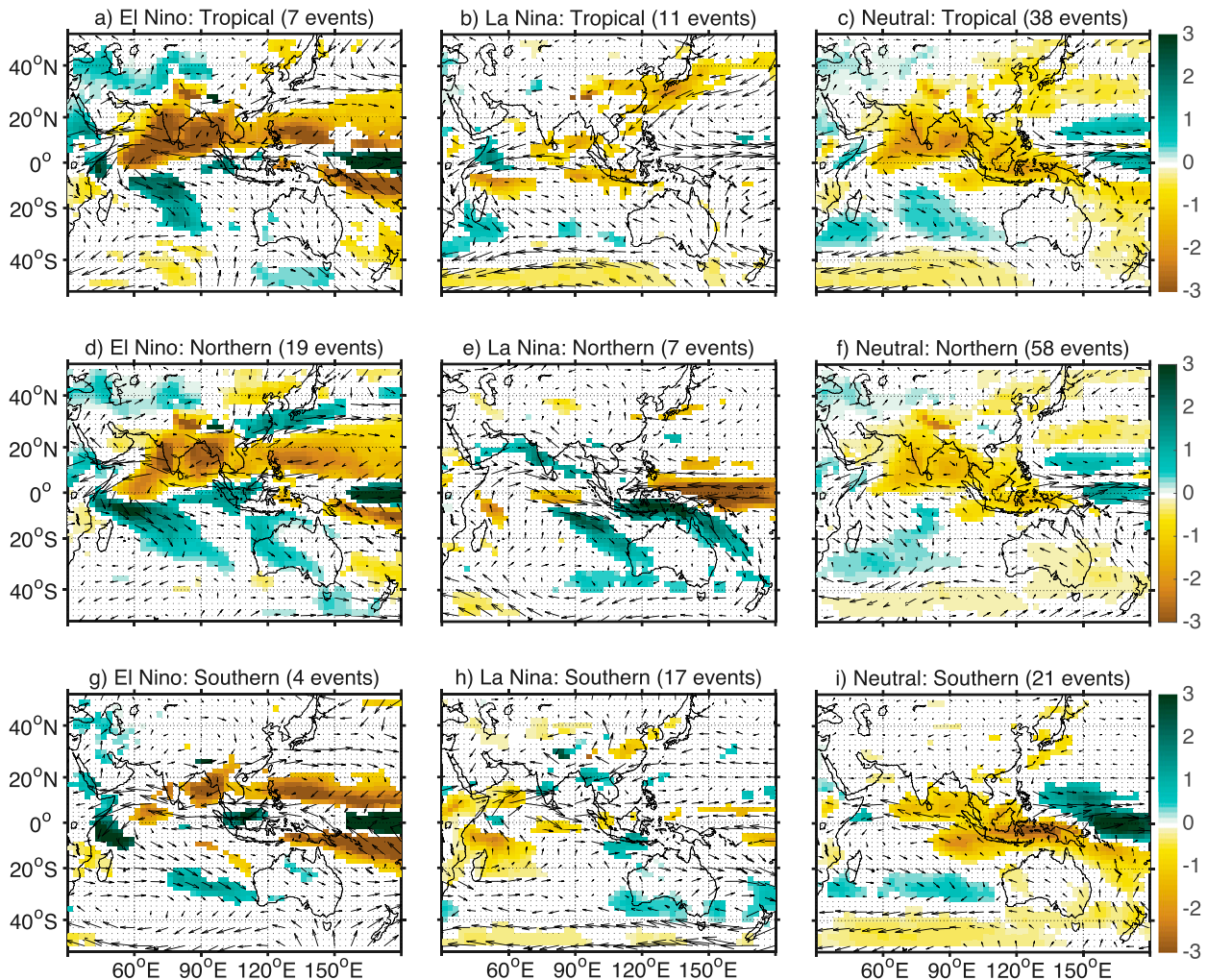


FIG. 10. Precipitation (mm day^{-1} ; colors) and 850-hPa wind (m s^{-1} ; arrows) anomalies for JJA +1, sorted by ENSO phase. (a), (d), (g) El Niño, (b), (e), (h) La Niña, and (c), (f), (i) ENSO neutral, for tropical, northern, and southern eruptions, respectively. Only values plotted are those where differences in precipitation between selected years and the ensemble mean are significant at 90%, according to the Wilcoxon rank-sum test. Stippling elsewhere indicates differences insignificant at 90%.

El Niño occurrences, which could potentially mask the significance of an initial La Niña-like response.

- 5) Dating uncertainty in the proxy record—offsets between reconstructed eruption years have been previously documented [cf. Gao et al. (2008) versus Crowley et al. (2008) and Sigl et al. (2015)] and could affect the composites; we do not expect this effect to be very large, as Anchukaitis et al. (2010) found little sensitivity of eruption-year hydroclimate composites to the set of eruption years considered. Persistence biases in tree-ring width-based reconstructions could potentially also play a role, as ring width may not always respond quickly to eruptions (Schneider et al. 2015).
- 6) Internal variability in the proxy record—proxy reconstructions contain only a single realization of internal variability, that which occurred in the real

climate system; as such, if La Niña occurrence were present during an unusually high proportion of eruption years, this could cause some of the eruption-year discrepancy.

- 7) Actual errors in model physics—the assessment of tree-ring-derived eruption responses in Anchukaitis et al. (2010) cited issues with monsoon representation in climate models as the primary source of model/proxy discrepancies, based on the robustness of the proxy data and the lack of a La Niña-like monsoon signal in three different model versions. Issues with monsoon representation in CESM cannot be ruled out as contributing to this disagreement. However, the wetter eruption-year conditions over North America in the NADA suggests that the issue may also lie with ENSO dynamics (McGregor et al.

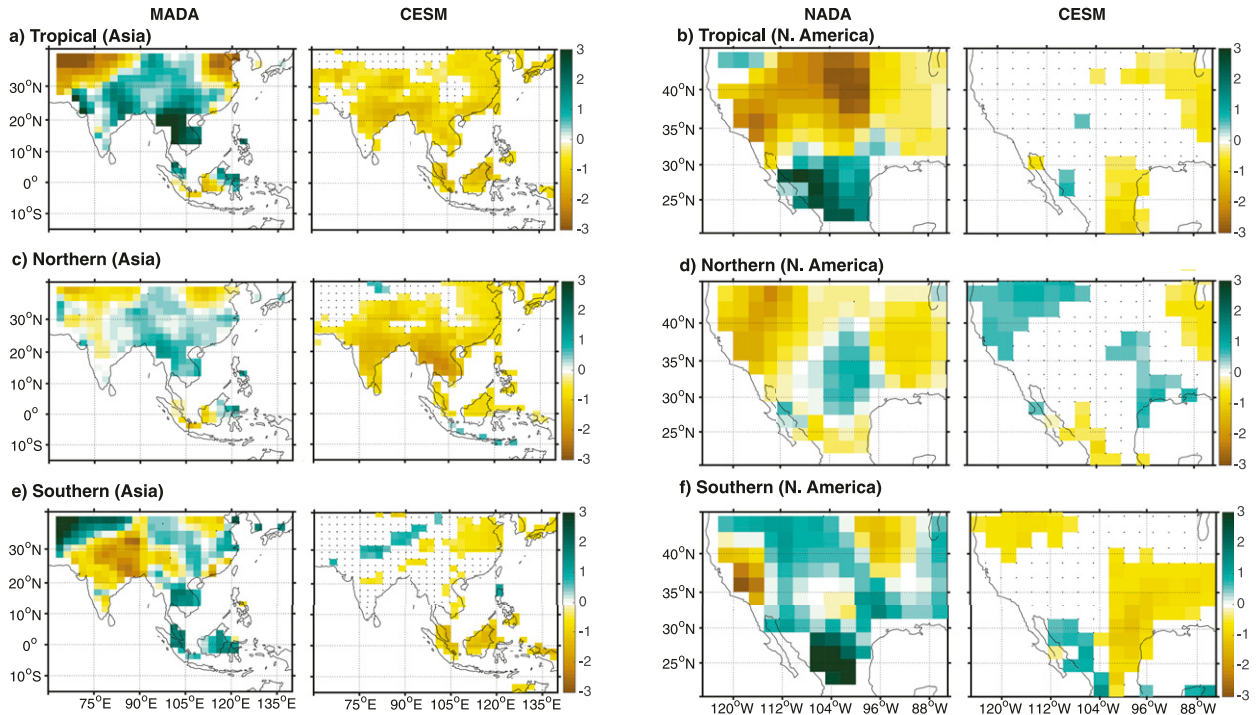


FIG. 11. PDSI anomaly composites for JJA +0 for the LME simulations compared with the North American and monsoon Asia drought atlases. Tropical eruptions for (a) Southeast Asia and (b) North America (c),(d) As in (a),(b), but for Northern eruptions. (e),(f) As in (a),(b), but for Southern eruptions. Eruption years used for compositing are identical between the CESM and the NADA/MADA. Stippling in both the CESM and NADA/MADA panels indicates posteruption PDSI composites, which are not significantly different from internal variability within the LME (nearly nowhere in NADA/MADA).

2010), rather than being strictly related to monsoon processes.

Of the above list, addressing model error is the most urgent for the climate modeling community, as determining areas where models fail to capture physical processes is a key requirement for improving future projections. However, until options 1–5 have been ruled out it will be difficult, if not impossible, to definitively attribute improved agreement with the proxy record to improvements in model physics.

This work also serves to demonstrate the urgent need for future data collection efforts. The regions with the highest proxy data density are also those with the strongest similarity between ENSO-neutral eruption and El Niño teleconnection patterns. This implies that obtaining additional well-dated records from other regions will be valuable for separately validating models' ability to represent the magnitude of the "direct" volcanic influence and the effects of volcanism on ENSO, with the caveat that these comparisons should be restricted to locations where the model is able to correctly capture the ENSO teleconnection for the historical period. Another critical data gap at present is found in high-resolution SST records; obtaining better estimates

of SST prior to large volcanic eruptions would provide crucial insights into the relative contribution of oceanic versus aerosol-induced hydroclimate anomalies.

6. Conclusions

This work uses the CESM Last Millennium Ensemble to investigate the separate influences of volcanic eruptions and ENSO on hydroclimate variability. The overall reduction in solar radiation incident at the surface leads to worldwide cooling in CESM after eruptions, which is enhanced at high latitudes but persists for 2–3 yr even in the tropics. Responses are generally strongest in the hemisphere of maximum aerosol loading, with a more symmetric response to Tropical eruptions. Very little tendency for El Niño or La Niña initiation is observed during the winter of Tropical eruption years; however, Northern eruptions show a weak but distinct El Niño-like pattern during DJF of years +0 to +1, whereas a generalized cooling occurs during Southern eruption winters. Both Tropical and Northern eruptions favor El Niño development during DJF +1 to +2, which is not observed for Southern eruptions.

Eruptions are separated into groups according to whether El Niño, La Niña, or ENSO-neutral conditions followed

during winters of years +0 to +1 or +1 to +2. The general tendency is for El Niño occurrence to magnify the hydroclimate impact of a given eruption in monsoon Asia and the southwest United States, and for La Niña occurrence to weaken or reverse the impact. This is shown to result from a similarity between the patterns associated with direct volcanic forcing and with El Niño, which occur as a result of a variety of distinct dynamical mechanisms. There is congruence between the anomalous meridional temperature gradient: high-latitude cooling during an eruption and equatorial heating during an El Niño both enhance this gradient, leading to an equatorward shift and slight acceleration of the mid-latitude westerly jet. The Asian monsoon is also suppressed by both eruptions and El Niño, because of an anomalous northeasterly flow off the coast of China (volcano only) and suppression of convection over the warm pool by a weaker Walker circulation (El Niño only). The resemblance between direct volcanic impacts and El Niño events implies that an El Niño-like response documented in the SW United States and/or monsoon Asia does not necessarily require an El Niño-like SST anomaly in all cases; however, substantial offsets between “volcano only” and El Niño-induced anomalies do exist in other regions.

Model results are compared with tree-ring reconstructions of hydroclimate to assess CESM performance. The largest disagreements are seen during the eruption year itself: all eruption classes lead to Asian monsoon suppression in CESM, where composites based on the MADA indicate an increase. In North America, Northern eruptions create wetting in the CESM and drying in the NADA, while the opposite is true for Southern eruptions. This suggests that CESM may not correctly capture either the ENSO or direct aerosol response during the year of the eruption. Possible explanations also include issues with the eruption-year aerosol transport, or with the seasonality of eruptions [all eruptions with unknown seasonality are assumed to begin in April in the Gao et al. (2008) reconstruction]; internal variability in the proxy record may also play a role. This work serves to highlight the critical importance of marine proxy reconstructions for attribution of model/proxy offsets to issues with particular simulated physical processes.

Acknowledgments. This work is supported by an NSF EaSM grant (AGS 1243125). The CESM project is supported by the National Science Foundation and the Office of Science (Biological and Environmental Research program) of the U.S. Department of Energy. Computing resources were provided by the Climate Simulation Laboratory at NCAR's Computational and Information Systems Laboratory (CISL), which is sponsored by the National Science Foundation and other agencies.

REFERENCES

- Adams, J. B., M. E. Mann, and C. M. Ammann, 2003: Proxy evidence for an El Niño-like response to volcanic forcing. *Nature*, **426**, 274–278, doi:10.1038/nature02101.
- Anchukaitis, K. J., B. M. Buckley, E. R. Cook, B. I. Cook, R. D. D'Arrigo, and C. M. Ammann, 2010: Influence of volcanic eruptions on the climate of the Asian monsoon region. *Geophys. Res. Lett.*, **37**, L22703, doi:10.1029/2010GL044843.
- Berger, A., 1978: Long-term variations of daily insolation and quaternary climatic changes. *J. Atmos. Sci.*, **35**, 2362–2367, doi:10.1175/1520-0469(1978)035<2362:LTVOI>2.0.CO;2.
- Clement, A. C., R. Seager, M. A. Cane, and S. E. Zebiak, 1996: An ocean dynamical thermostat. *J. Climate*, **9**, 2190–2196, doi:10.1175/1520-0442(1996)009<2190:AODT>2.0.CO;2.
- Cook, B. I., T. R. Ault, and J. E. Smerdon, 2015: Unprecedented 21st century drought risk in the American southwest and central plains. *Sci. Adv.*, **1**, e1400082, doi:10.1126/sciadv.1400082.
- Cook, E., C. Woodhouse, C. Eakin, D. Meko, and D. Stahle, 2004: Long-term aridity changes in the western United States. *Science*, **306**, 1015–1018, doi:10.1126/science.1102586.
- , K. Anchukaitis, B. Buckley, R. D'Arrigo, G. Jacoby, and W. Wright, 2010: Asian monsoon failure and megadrought during the last millennium. *Science*, **328**, 486–489, doi:10.1126/science.1185188.
- Crowley, T. J., G. Zielinski, B. Vinther, R. Udisti, K. Kreutz, J. Cole-Dai, and E. Castellano, 2008: Volcanism and the Little Ice Age. *PAGES Newsletter*, Vol. 16, No. 2, 22–23. [Available online at http://www.geology.um.maine.edu/publications/Crowley_PAGES_2008.pdf.]
- Emile-Geay, J., R. Seager, M. A. Cane, E. R. Cook, and G. H. Haug, 2008: Volcanoes and ENSO over the past millennium. *J. Climate*, **21**, 3134–3148, doi:10.1175/2007JCLI1884.1.
- Gao, C. C., A. Robock, and C. Ammann, 2008: Volcanic forcing of climate over the past 1500 years: An improved ice core-based index for climate models. *J. Geophys. Res.*, **113**, D23111, doi:10.1029/2008JD010239.
- Grieser, J., and C. D. Schonwiese, 1999: Parameterization of spatiotemporal patterns of volcanic aerosol induced stratospheric optical depth and its climate radiative forcing. *Atmosfera*, **12**, 111–133.
- Hurt, G. C., and Coauthors, 2011: Harmonization of land-use scenarios for the period 1500–2100: 600 years of global gridded annual land-use transitions, wood harvest, and resulting secondary lands. *Climatic Change*, **109**, 117–161, doi:10.1007/s10584-011-0153-2.
- Jacobi, J., D. Perrone, L. L. Duncan, and G. Hornberger, 2013: A tool for calculating the Palmer drought indices. *Water Resour. Res.*, **49**, 6086–6089, doi:10.1002/wrcr.20342.
- Kang, S. M., I. M. Held, D. M. W. Frierson, and M. Zhao, 2008: The response of the ITCZ to extratropical thermal forcing: Idealized slab-ocean experiments with a GCM. *J. Climate*, **21**, 3521–3532, doi:10.1175/2007JCLI2146.1.
- Kay, J. E., and Coauthors, 2015: The Community Earth System Model (CESM) Large Ensemble Project: A community resource for studying climate change in the presence of internal climate variability. *Bull. Amer. Meteor. Soc.*, **96**, 1333–1349, doi:10.1175/BAMS-D-13-00255.1.
- Knudsen, M. F., B. H. Jacobsen, M.-S. Seidenkrantz, and J. Olsen, 2014: Evidence for external forcing of the Atlantic multi-decadal oscillation since termination of the Little Ice Age. *Nat. Commun.*, **5**, 3323, doi:10.1038/ncomms4323.

- Kumar, K. K., B. Rajagopalan, M. Hoerling, G. Bates, and M. Cane, 2006: Unraveling the mystery of Indian monsoon failure during El Niño. *Science*, **314**, 115–119, doi:[10.1126/science.1131152](https://doi.org/10.1126/science.1131152).
- Landrum, L., B. Otto-Bliesner, E. R. Wahl, A. Conley, P. J. Lawrence, N. Rosenbloom, and H. Teng, 2013: Last millennium climate and its variability in CCSM4. *J. Climate*, **26**, 1085–1111, doi:[10.1175/JCLI-D-11-00326.1](https://doi.org/10.1175/JCLI-D-11-00326.1).
- Li, J., and Coauthors, 2013: El Niño modulations over the past seven centuries. *Nat. Climate Change*, **3**, 822–826, doi:[10.1038/nclimate1936](https://doi.org/10.1038/nclimate1936).
- Maher, N., A. Sen Gupta, and M. H. England, 2014: Drivers of decadal hiatus periods in the 20th and 21st centuries. *Geophys. Res. Lett.*, **41**, 5978–5986, doi:[10.1002/2014GL060527](https://doi.org/10.1002/2014GL060527).
- McGregor, S., and A. Timmermann, 2011: The effect of explosive tropical volcanism on ENSO. *J. Climate*, **24**, 2178–2191, doi:[10.1175/2010JCLI3990.1](https://doi.org/10.1175/2010JCLI3990.1).
- , —, and O. Timm, 2010: A unified proxy for ENSO and PDO variability since 1650. *Climate Past*, **6**, 1–17, doi:[10.5194/cp-6-1-2010](https://doi.org/10.5194/cp-6-1-2010).
- Mignot, J., M. Khodri, C. Frankignoul, and J. Servonnat, 2011: Volcanic impact on the Atlantic Ocean over the last millennium. *Climate Past*, **7**, 1439–1455, doi:[10.5194/cp-7-1439-2011](https://doi.org/10.5194/cp-7-1439-2011).
- Otto-Bliesner, B., and Coauthors, 2015: Climate variability and change since 850 CE: An ensemble approach with the Community Earth System Model (CESM). *Bull. Amer. Meteor. Soc.*, doi:[10.1175/BAMS-D-14-00233.1](https://doi.org/10.1175/BAMS-D-14-00233.1), in press.
- Palmer, W. C., 1965: Meteorological drought. U.S. Weather Bureau Research Paper 45, 58 pp. [Available online at <https://www.ncdc.noaa.gov/temp-and-precip/drought/docs/palmer.pdf>.]
- Pongratz, J., T. Raddatz, C. H. Reick, M. Esch, and M. Claussen, 2009: Radiative forcing from anthropogenic land cover change since AD 800. *Geophys. Res. Lett.*, **36**, L02709, doi:[10.1029/2008GL036394](https://doi.org/10.1029/2008GL036394).
- Robock, A., 2000: Volcanic eruptions and climate. *Rev. Geophys.*, **38**, 191–219, doi:[10.1029/1998RG000054](https://doi.org/10.1029/1998RG000054).
- Schmidt, G. A., and Coauthors, 2011: Climate forcing reconstructions for use in PMIP simulations of the last millennium (v1.0). *Geosci. Model Dev.*, **4**, 33–45, doi:[10.5194/gmd-4-33-2011](https://doi.org/10.5194/gmd-4-33-2011).
- Schneider, D. P., C. M. Ammann, B. L. Otto-Bliesner, and D. S. Kaufman, 2009: Climate response to large, high-latitude and low-latitude volcanic eruptions in the Community Climate System Model. *J. Geophys. Res.*, **114**, D15101, doi:[10.1029/2008JD011222](https://doi.org/10.1029/2008JD011222).
- Schneider, L., J. E. Smerdon, U. Buntgen, R. J. S. Wilson, V. S. Myglan, A. V. Kirdyanov, and J. Esper, 2015: Revising mid-latitude summer temperatures back to A.D. 600 based on a wood density network. *Geophys. Res. Lett.*, **42**, 4556–4562, doi:[10.1002/2015GL063956](https://doi.org/10.1002/2015GL063956).
- Seager, R., N. Harnik, Y. Kushnir, W. Robinsin, and J. Miller, 2003: Mechanisms of hemispherically symmetric climate variability. *J. Climate*, **16**, 2960–2978, doi:[10.1175/1520-0442\(2003\)016<2960:MOHSCV>2.0.CO;2](https://doi.org/10.1175/1520-0442(2003)016<2960:MOHSCV>2.0.CO;2).
- Sigl, M., and Coauthors, 2014: Insights from Antarctica on volcanic forcing during the common era. *Nat. Climate Change*, **4**, 693–697, doi:[10.1038/nclimate2293](https://doi.org/10.1038/nclimate2293).
- , and Coauthors, 2015: Timing and climate forcing of volcanic eruptions for the past 2,500 years. *Nature*, **523**, 543–549, doi:[10.1038/nature14565](https://doi.org/10.1038/nature14565).
- Smith, T., R. W. Reynolds, T. C. Peterson, and J. Lawrimore, 2008: Improvements to NOAA's historical merged land–ocean surface temperature analysis (1880–2006). *J. Climate*, **21**, 2283–2296, doi:[10.1175/2007JCLI2100.1](https://doi.org/10.1175/2007JCLI2100.1).
- Stommel, H., and E. Stommel, 1983: *Volcano Weather: The Story of 1816, the Year Without a Summer*. Seven Seas Press, 177 pp.
- Stothers, R. B., 1984: The great Tambora eruption in 1815 and its aftermath. *Science*, **224**, 1191–1198, doi:[10.1126/science.224.4654.1191](https://doi.org/10.1126/science.224.4654.1191).
- Timmreck, C., 2012: Modeling the climatic effects of large explosive volcanic eruptions. *Wiley Interdiscip. Rev.: Climate Change*, **3**, 545–564, doi:[10.1002/wcc.192](https://doi.org/10.1002/wcc.192).
- Vieira, L. E. A., S. K. Solanki, N. A. Krivova, and I. Usoskin, 2010: Evolution of the solar irradiance on time scales of years to millennia. *Astron. Astrophys.*, **509**, A100, doi:[10.1051/0004-6361/200913276](https://doi.org/10.1051/0004-6361/200913276).
- Wahl, E. R., H. F. Diaz, J. E. Smerdon, and C. M. Ammann, 2014: Late winter temperature response to large tropical volcanic eruptions in temperate western North America: Relationship to ENSO phases. *Global Planet. Change*, **122**, 238–250, doi:[10.1016/j.gloplacha.2014.08.005](https://doi.org/10.1016/j.gloplacha.2014.08.005).
- Zanchettin, D., C. Timmreck, H.-F. Graf, A. Rubino, S. Lorenz, K. Lohmann, K. Krueger, and J. H. Jungclaus, 2012: Bi-decadal variability excited in the coupled ocean–atmosphere system by strong tropical volcanic eruptions. *Climate Dyn.*, **39**, 419–444, doi:[10.1007/s00382-011-1167-1](https://doi.org/10.1007/s00382-011-1167-1).